# Influence of colloidal surface-additivation with low melting point metal nanoparticles on Nd-Fe-B permanent magnets produced by suction casting

Jianing Liu[1], Ying Yang[2], Franziska Staab[3], Carlos Doñate-Buendia[4], René Streubel[2], Bilal Gökce[4], Fernando Macarri[1], Philipp Gabriel[2], Benjamin Zingsem[5], Detlef Spoddig[5], Konstantin Skokov[1], Oliver Gutfleisch[1], Michael Farle[5], Stephan Barcikowski[2*], Anna Rosa Ziefuss[2]

[1] Functional Materials, Institute of Material Science, Technical University of Darmstadt, 64287 Darmstadt, Germany

[2] Technical Chemistry and Center for Nanointegration Duisburg-Essen (CENIDE), University of Duisburg-Essen, 45141 Essen, Germany

[3] Physical Metallurgy, Institute of Material Science, Technical University of Darmstadt, 64287 Darmstadt, Germany

[4] Materials Science and Additive Manufacturing, School of Mechanical Engineering and Safety Engineering, University of Wuppertal, 42119 Wuppertal, Germany

[5] Faculty of Physics and Center for Nanointegration Duisburg-Essen (CENIDE), University of Duisburg-Essen, 47048 Duisburg, Germany

* corresponding author: stephan.barcikowski@uni-due.de

Keywords:

Magnetic properties
Hard magnets
Additive Manufacturing
Laser ablation in liquid
Grain boundary diffusion
Microstructure

**Abstract**

The development of new powder feedstocks using nanoparticles (NPs) has the potential to enhance the functionality of as-built parts and overcome the limitations of current additive manufacturing (AM) techniques. This study investigated the impact of NP feedstock modification on the microstructure and functionality of MQP-S after suction casting. Two types of NPs, Ag, and $ZrB_2$, were used, and their effects on grain size distribution and dendritic structure were evaluated. Ag NPs resulted in smaller, more uniform grain sizes and increased functionality, but only for loadings > 0.5 monolayers. $ZrB_2$ resulted in uniformly distributed grain sizes at much lower mass loadings, with even more compact dendritic arms. However, no effect on functionality was observed. The results show that feedstock modification with low melting point metal NPs can improve the microstructure and magnetic properties of permanent magnets produced by AM and highlight the potential of using NPs to develop new powder feedstocks for AM. With this, it provides insights for future research on optimizing AM processes.

## Introduction

Lasers in production offer flexibility in shape design, reduced material loss, and the possibility of industrial-scale production [1][2]. However, although they are becoming increasingly powerful and brilliant, the materials available are often completely inadequate for the processing tasks currently required. In laser-based additive manufacturing (AM), the material variability is limited due to complex sintering and melting mechanisms during processing, which leads to process instabilities, porosities, and other defects in the as-built parts [3]. Therefore, there is an urgent need to adapt the materials to these widespread production processes, as AM will dominate important production processes in the long term due to their throughput and precision.

Powder bed fusion using a laser beam (PBF-LB) is one of the most prominent AM techniques. Here, a laser beam completely melts the metal feedstocks to obtain fully dense parts after solidification [4]. However, extremely high solidification rates in the range of $10^5$ K/s [5] of the molten metal feedstock may lead to micro-cracks, non-equilibrium microstructure with phase segregation, and columnar grain growth, in most cases, will influence the material strength [5]. In AlSi10Mg alloys, the fast-cooling rates result in an ultrafine supersaturated Si-rich network inside each grain which positively influences the corrosion behavior; however, strong residual stresses and microstructural inhomogeneities negatively affect further mechanical properties like ductility and fatigue resistance [6][7][8]. Yet, compared with structural materials (e.g., 316L, AlSi10Mg, and Ti6Al4V), functional materials like shape memory alloys (e.g., Ni-Mn-In or Co-Ni-Ga) or permanent magnets (PM) based on rare earth elements (e.g., Nd-Fe-B) are rarely produced with AM, and further research is necessary to correlate the melting-induced microstructures with the functional read-out in as-build parts [9][10]. The desirable microstructure for high coercivity in, e.g., Nd-Fe-B alloys consists of $Nd_2Fe_{14}B$ grains isolated by a paramagnetic grain boundary phase [11]. However, if high thermal gradients occur during re-solidification, a dendritic microstructure may form, negatively affecting magnetic properties [12][13]. Moreover, an uneven distribution of grain size can also have an adverse effect on coercivity [14]. Thus, further research is necessary to fully comprehend the microstructure and optimize manufacturing permanent magnets using advanced techniques.

A fundamental research approach already at the beginning of the process chain, the feedstock power, is required. In the past decade, research has shown that using nanoparticles (NPs) for feedstock modification can address processability limitations and improve the properties of as-built parts [15][16]. Nonetheless, current research on NP-based feedstock modification focuses on non-functional materials, highlighting the need for comprehensive research on such mater, including the entire process chain, powder feedstock, processing, microstructure, and part properties. Here suction casting is an ideal test bench [11], as it requires only a few grams of feedstocks, allowing the fast processing of different feedstock modifications. The powder is melted and sucked into a water-cooling mold to simulate the high cooling rate of PBF-LB, a similar microstructure, and the same existing phases can be achieved.

This study utilized laser-generated Ag and $ZrB_2$ NPs to modify a rare-earth-based feedstock material. Studies have demonstrated that incorporating Ag into Nd-based magnets can enhance their functional properties after processing with conventional sintering techniques [15] [16]. Since Ag has a lower melting point than Nd-Fe-B, it can rapidly melt and fill in any vacant spaces in the loosely packed powder layers of the PBF-LB/M process, resulting in a higher packing density. This elevated packing density positively influences the final part density and, consequently, the magnetic performance. $ZrB_2$ NPs melt later than the original feedstock mater and are intended to remain solid during the melting of MQP-S and regulate grain growth during re-solidification. (mechanism II, Figure 1B)

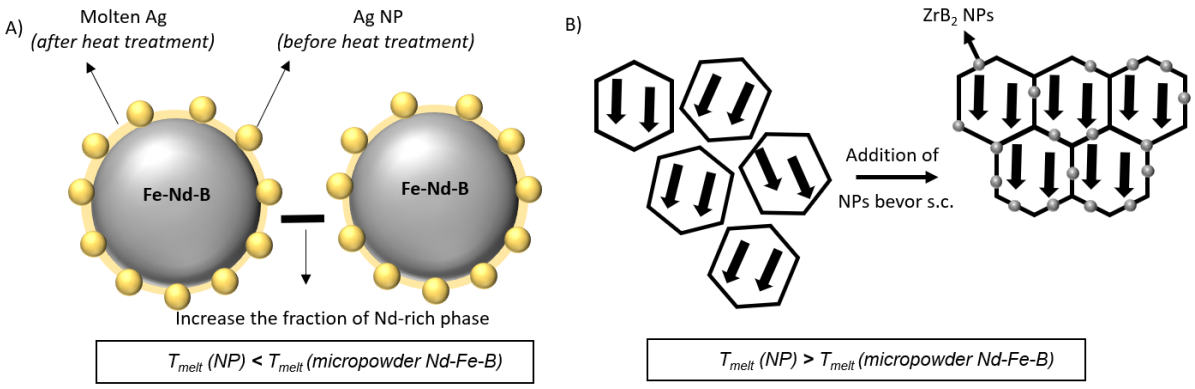


*Figure 1 Schematic description of the effect of adding nanoparticles on Nd-Fe-B. A)* **Mechanism I:** *Ag NPs decorated on the surface of Nd-Fe-B microparticles will melt and join the Nd-rich phase during solidification, increasing the Nd-rich phase's volume fraction and potentially assisting in decoupling the grains. B) $ZrB_2$ NPs will melt later (or not at all, dependent on process parameters) and resolidify earlier than the Nd-Fe-B, which enables the nanoparticles to act as additional starting points for grain growth, potentially leading to finer, equiaxed grains.*

## Results and Discussion

This study investigates the influence of NPs loading on the as-build part microstructure of functional material. We will concentrate on MQP-S, which is a commercially available permanent feedstock for processing [19][20]. However, strong temperature gradients will strongly reduce the functionality as unsuitable dendritic microstructures appear after AM processing [13].

### Feedstock modification

The production of NPs was done via laser ablation in liquids, enabling the synthesis of surfactant-free particles [21] without including any cross-effectors on the flowability, but at the same time providing good absorption probability [22]. Moreover, cross-effectors like organic residuals or colloidal stabilizers bear the risk of creating gases by laser vaporization. They may cause unwanted balling effects during processing, as has been shown for laser direct-writing of stabilizer-containing Ag microparticle inks [23], which should be avoided during processing. Detailed information on the NPs' production can be found in the method part. Although the particle size in both cases shows a monomodal distribution, the Ag NPs exhibit an average size of 8 nm, while the $ZrB_2$ NPs have an average size of 100 nm. (Figure 2A). Note that the differences in particle size are intended concerning the different natures of the targeted mechanisms. Mechanism 1 aims to investigate the impact of an NP shell, with greater precision in adjusting the shell diameter achievable when using small Ag NPs. Figure 2B shows the statistical difference between two Nd-Fe-B-based microparticles dependent on the Ag NPs mass-loading. Note that melting will decrease the packing density of Ag on the surface, resulting in partly lower values.

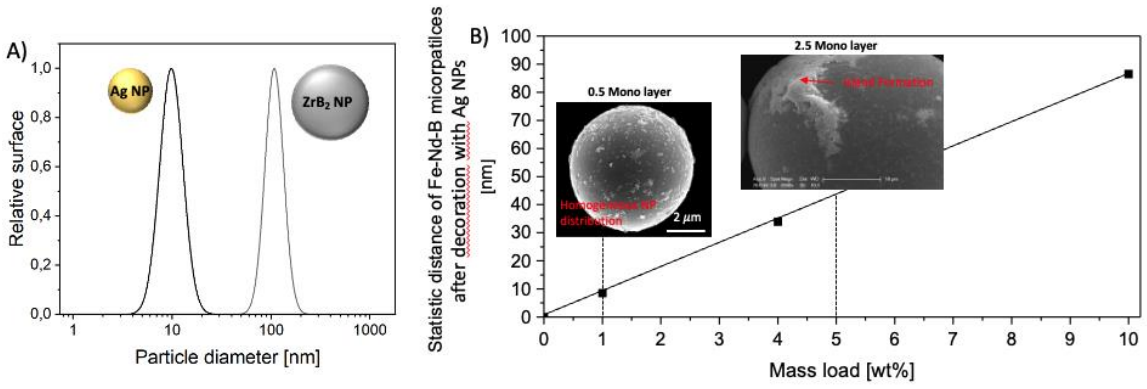

*Figure 2: A) Nanoparticle size distribution after laser-based production of Ag NPs (Black) and ZrB2 NPs (grey) curves. B) Calculated statistical distance of MQP-S powder in dependence on the mass load of Ag NPs. The calculation assumes sphericity for both NPs and MPs and was done using a mean NPs of 8 nm and a mean MPs size of 43 nm (size distribution of the MQP-S powder can be found in the SI).*

Mechanism II, however, accounts for larger particles to enable strong nucleation sizes. Here, we also varied the NPs mass loading on the MPs surface, providing the process with different nucleation centers. Here a mass loading of 1 wt.% enables roughly 968,000 nucleation centers.

As the Ag NPs were produced in water, we performed the surface decoration diffusion controlled by varying the pH value in the presence of the Ag NPs and Nd-Fe-B MPs. Note that the surface charges are a function of the pH value and that there is a pH range (pH 3-8) where both reagents show a different sign of the surface charge (zeta potential is negative for Ag [24] and positive for Nd-Fe-B MPs [25]). However, Nd-Fe-B tends to oxidize in the acidic range [26], so we carefully adjusted the pH value to 7-8. While lower mass loadings of Ag NPs are highly homogeneously distributed, larger amounts tend to form islands on the microparticle surface (see inset Figure 1B). Additionally, we calculated and confirmed via SEM analysis that supporting 1 wt.% of Ag NPs on the surface of MQP-S results statistically in 0.5 monolayer of Ag NPs, enabling a statistical distance between two MPs in the range of the NP's diameter. The $ZrB_2$ NPs were produced in ethanol, which disabled a diffusion-controlled absorption. Here, we evaporated the liquid in the presence of the feedstock, which will increase the concentration of both agents in time, promoting absorption processes.

**Powder processing and characterization of final parts**

After successfully modifying the feedstock powder, we processed seven Ag NPs modified feedstocks (0.1 – 10 wt.%) and four $ZrB_2$ modified feedstocks (0.1 – 2 wt.%) via suction casting, an ideal test bench for PBF-LB with small powder throughput [11]. As introduced, NPs are known to alter the as-build parts microstructure, which we visualized using EBSD, SEM-BSE, and SEM-EDX in the following. Note that we performed heat-treatment cycles prior to further analysis as this causes atomic diffusion and rearrangement of the crystal structure, promoting magnetic anisotropy and coercivity, resulting in stronger functionality [27].

Exemplary EBSD images of as-build parts, produced via suction casing, for pure MQP-S and MQP-S, additivated with Ag (0.1, 1, and 7 wt.%) or $ZrB_2$ (0.1 and 1 wt.%) NPs, are shown in Figure 3. As expected, the microstructure of pure MQP-S suffers significantly from the

production conditions (high-temperature gradients and fast cooling rates), resulting in a clearly in-homogeneous grain-size distribution (spots 1 and 2 in Figure 3A) containing grains with sizes far larger than 10 µm. The same applies to samples containing 0.1 and 1 wt.% of Ag (Figure 3 B-C). However, both spots show significantly smaller grains than the unmodified as-build part. The sample containing 7 wt.% of Ag NPs (Figure 3D) and the samples decorated with $ZrB_2$ NPs (Figure 3E-F) showed a more homogeneous microstructure. In all cases, the grains show a dendritic growth, making it difficult to extract grain size distributions.

In summary, the EBSD results demonstrate a significant impact of NP modification, which varies for the two types and is affected by the NP's loading. Raising the Ag NPs loading leads to more uniform grain sizes but at the expense of very small grain sizes. Note that the 7 wt.% sample possesses an inhomogeneous NP distribution on the feedstock powder prior to suction casting. We cannot exclude any effect of the support characteristics on the microstructure of the as-built part, which would be highly interesting to be revealed in future studies. Conversely, increasing the $ZrB_2$ loading with the same mass leads to a generally good uniformity of grain sizes, with increased size observed with an increased mass load. Note that there is a correlation between grain size and the functionality of permanent magnets [28].

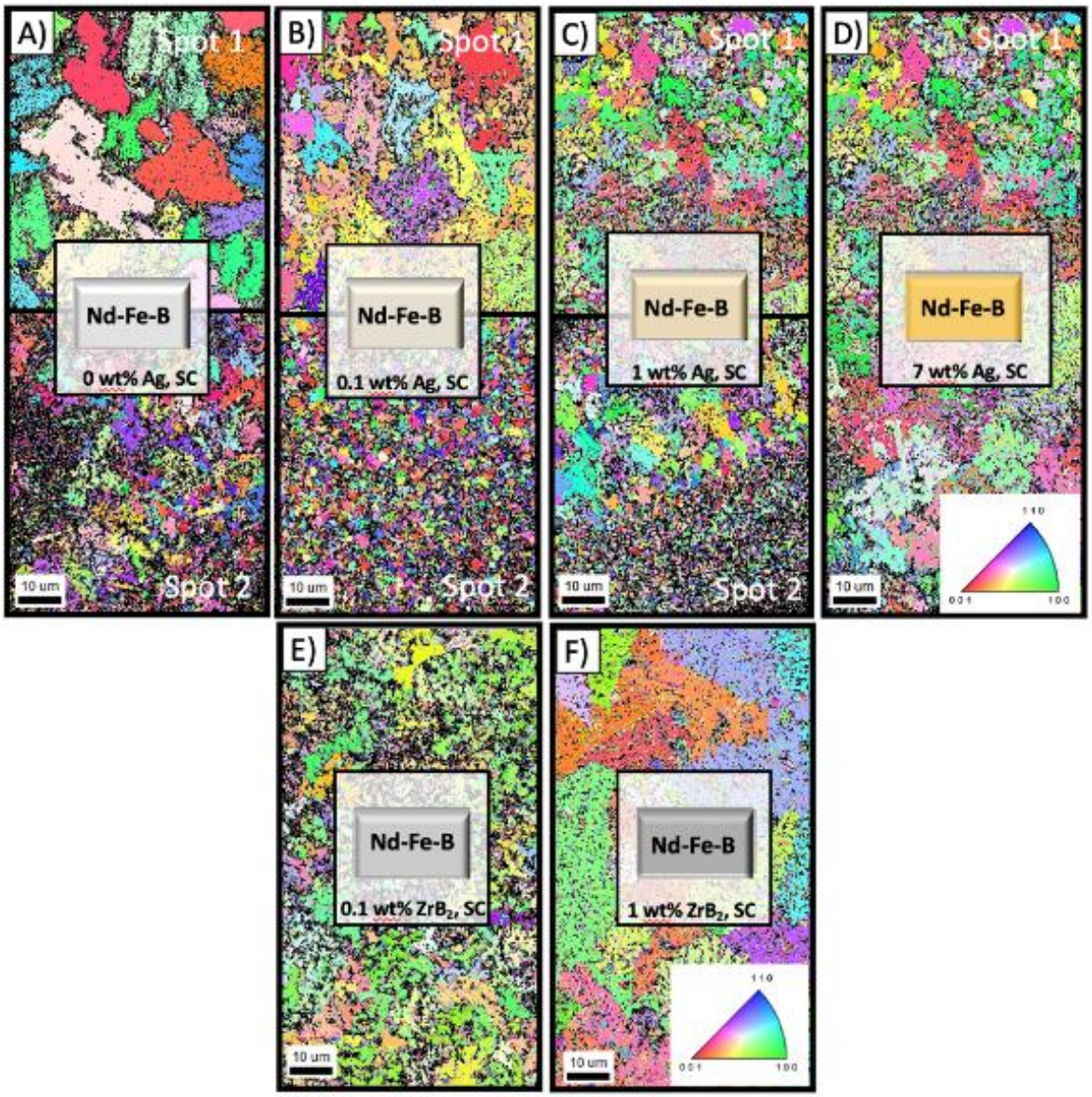


*Figure 3 EBSD images of annealed suction casting flakes from (A) non-modified (B-F) and modified MQP-S powders.*

Generally, the grain size closer to single domain size (~ 200 nm for $Nd_2Fe_{14}B$) lead to the maximal coercivity and optimal remanence [29]. However, there is a trade-off between grain size and other mechanical properties of the material, such as strength and toughness. Therefore, finding the optimal grain size for a given application requires a careful balance of magnetic and mechanical properties which is beyond the scope of the study.

Thus, we performed SEM-BSE to explore how different types of NPs affect grain size. One can see from Figure 4 that instead of small grains separated by a non-magnetic grain boundary phase, the dendritic structure forms in the samples. Dendritic arms are thin, finger-like projections that form during solidification [20]. It is known that such dendritic structure can

significantly affect the hard magnetic properties of Nd-Fe-B-based alloys [9][10][13][27]. As shown in Figure 4A, the microstructure of annealed suction-casting flakes from MQP-S powder is dendritic $Nd_2Fe_{14}B$ surrounded by α-iron as a grain boundary. Following [13], the nanocrystalline structure from the raw powder was destroyed during the remelting in the suction casting process, and the microstructure is much coarser afterwards. Figure 4B reveals the dendritic structure for one selected Ag NPs modified as-build part. The dendritic structure is much finer and more homogeneous, which can also be observed for the $ZrB_2$-modified as-build parts. Here, we resolved the dendritic structure for parts with increasing $ZrB_2$ amount and found the increasing density of dendritic arms with increasing NP content.

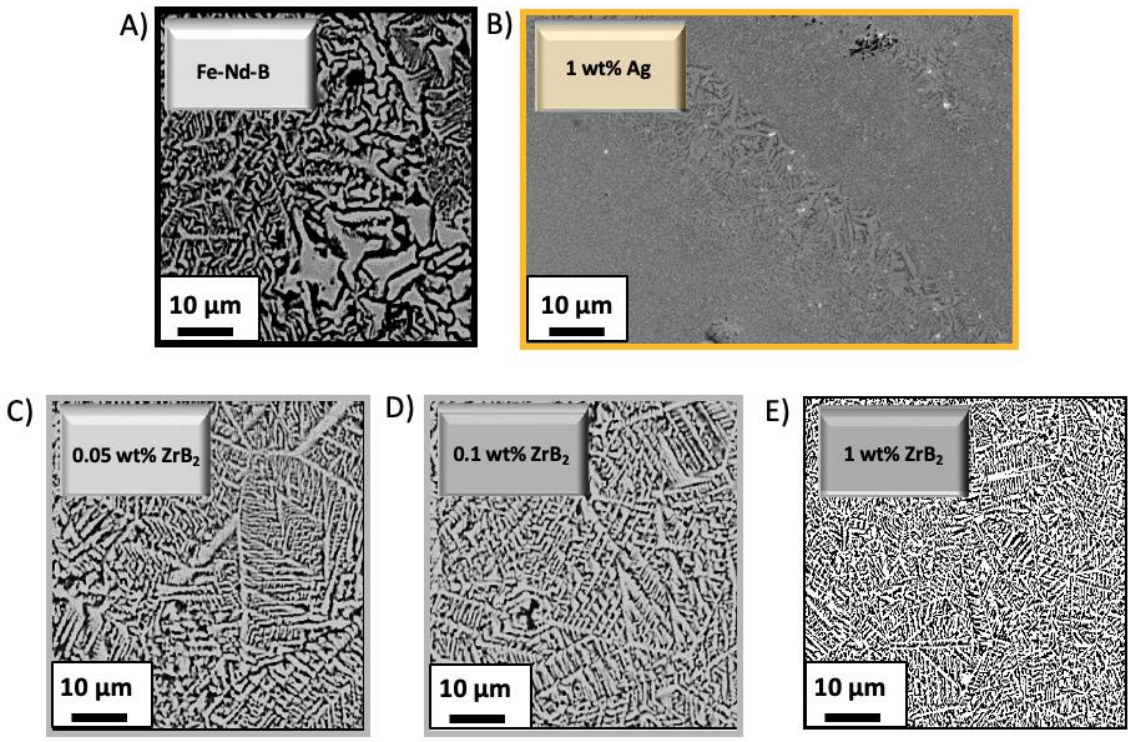


*Figure 4: SEM-BSE images of annealed suction casting flakes from A) unmodified MQP-S feedstock, B) modified feedstock with 1 wt.% Ag NPs, C) modified feedstock with 0.05 wt.% $ZrB_2$ NPs, D) modified feedstock with 0.1 wt.% $ZrB_2$ NPs, E) modified feedstock with 1 wt.% $ZrB_2$ NPs.*

Exemplary SEM-EDX analysis (Figure 5) was performed to visualize the distribution of NPs in the suction casted parts before assessing their functionality. The focus was primarily on the sample containing 1 wt.% Ag NPs and or $ZrB_2$ NPs. Despite the strongly homogeneous Ag NPs distribution resulting after feedstock modification (Figure 2B), the NPs were highly non-uniform in the as-built part, with silver mostly concentrated on elevated regions, suggesting

the presence of unmolten powder residues. However, the molten areas contained hardly any Ag or had amounts below the EDX's resolution limit.

Interestingly, areas with Ag had a significantly reduced percentage of Fe. Although it is unlikely for Ag to enter the $Nd_2Fe_{14}B$ matrix, it could potentially form intermetallic phases with Nd (not detected by EDX) [17], which our study neither confirms nor negates. In comparison, Zr is wide and more evenly distributed. As shown in Figure 4 D), due to the light color intensity (compared with Ag), no islands are observed, and it may enter the $Nd_2Fe_{14}B$ matrix, and we cannot exclude that it stabilizes the $Nd_2Fe_{17}$ phase simultaneously, thereby reducing the functionality. It has to be noted here that since B could not be precisely detected from EDX, only Zr is tracked. It is insufficient to confirm whether the Zr is from NPs additivation or the original alloying element in the raw MQP-S powder.

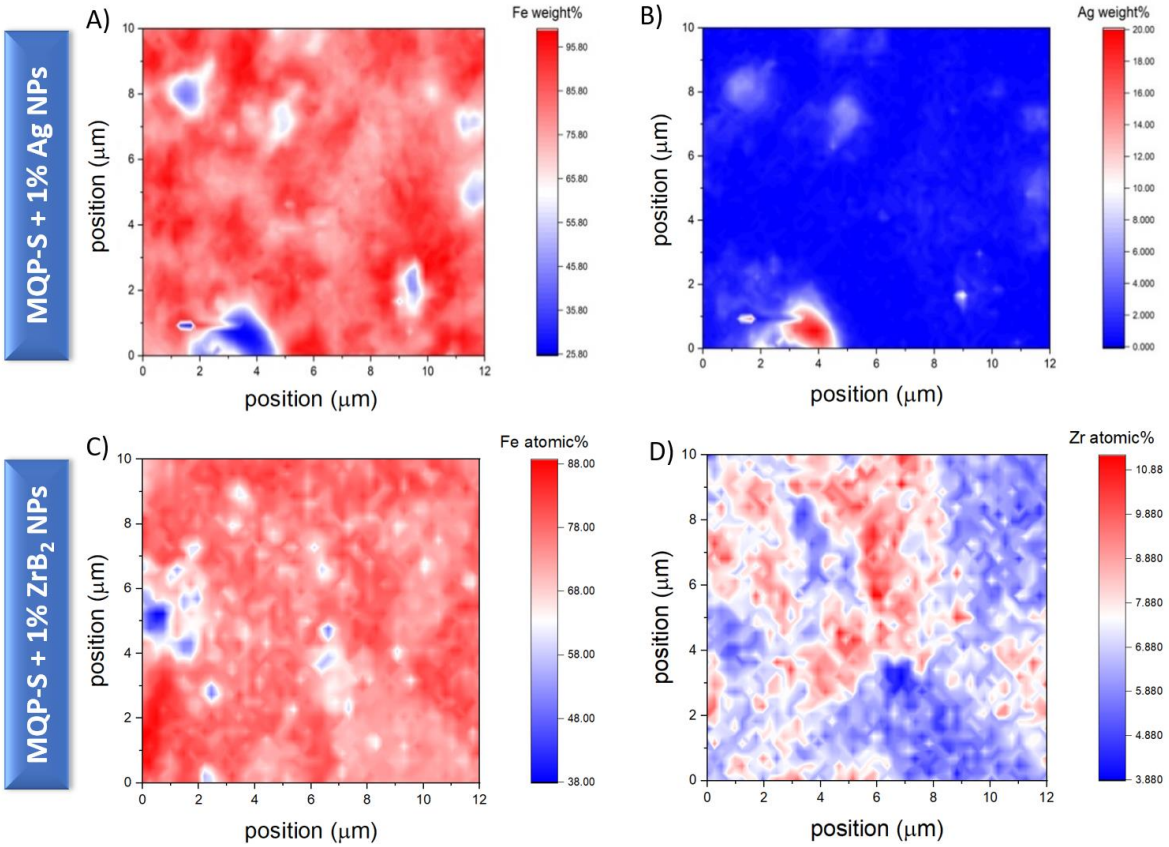


*Figure 4: EDX mapping of annealed suction casting flakes made by the produced powder feedstocks. (A) and (B) show the mapping of elements Fe and Ag in the sample from Ag NPs decorated MQP-S powder; (C) and (D) show the mapping of elements Fe and Zr in the sample from $ZrB_2$ NPs decorated MQP-S powder.*

As the microstructure is a decisive influence factor for the functionality of the MQP-S as build parts, we measured the magnetic properties using a vibrating sample magnetometer to reveal

hysteresis loops. Figure 5 shows extracted magnetic properties (coercivity and remanence) for heat treated suction casted samples decorated with Ag NPs (grey) and $ZrB_2$ NPs (green) in different mass-loadings and compared to the respective values of the raw powder after heat treatment (orange). These despair values are employed to find a dependency of the NPs' load on the permanent magnetic properties of the as-built parts. As expected from Literature [13][20][31], the initial material has totally lost its functionality showing a remanence of 0.29 T and a coercivity of less than 50 KA/m. Although $ZrB_2$ shows a more homogeneous grain size distribution and dense dendritic structure, we do not observe any influence on the functionality independent of the NPs mass loading. As mentioned above, we cannot exclude that Zr stabilizes $Nd_2Fe_{17}$, which is harmful to the hard magnetic properties and needs to be investigated for further studies. However, the Ag NPs $\geq$ 1 wt.% show a huge impact on the functionality showing a 150% increase in coercivity and a 100% increase in remanence. Note that the remanence increases to 0.45 T, which is only 25 % below the physical limit of the material. There is no statistically significant change in the strength of influence observed for mass loadings greater than 1 wt.%. A mass loading of 1 wt.% corresponds to a feedstock decoration of 0.5 monolayers (as explained earlier), which limits the statistical distance between two micro particles to the size of the NPs.

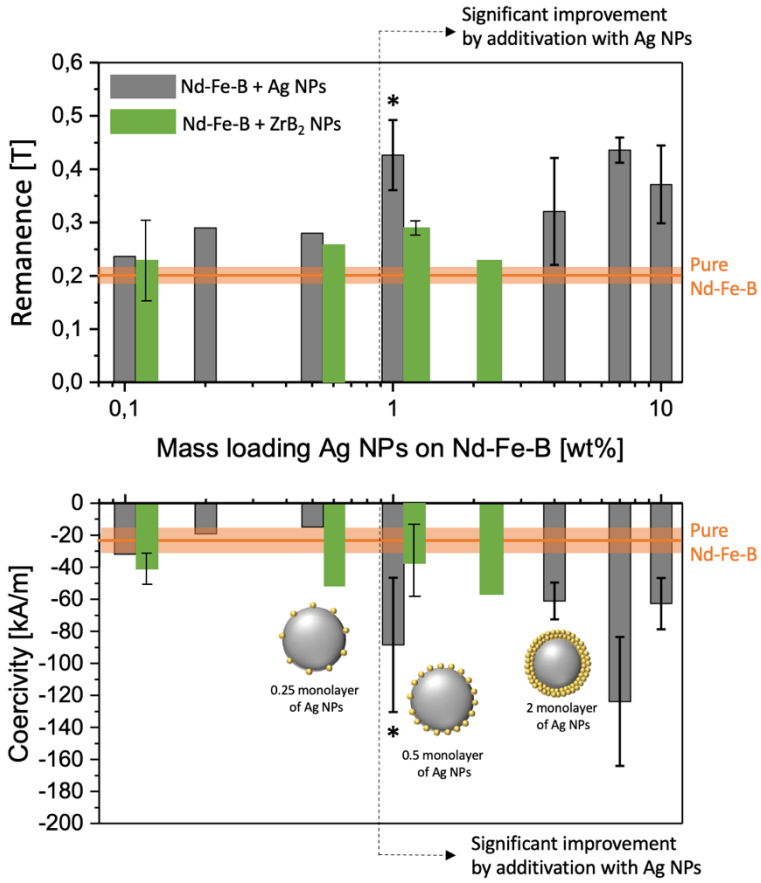


*Figure 5: Hysteresis curve of the initial Fe-Nd-B feedstock, including data after supporting 1, 4, 10 wt.% Ag NP on the microparticle surface. Data are collected after the suction casting of the produced powder feedstocks. Remanence (B) and Coercivity (C) are extracted and plotted depending on the statistical difference of the single Nd-Fe-B particles after heat treatment.*

## Summary and Conclusion

In summary, this research explored how modifying NP feedstock affected the microstructure and functionality of MQP-S after suction casting. Ag and $ZrB_2$ were used as two different types of NPs. Ag NPs were expected to melt earlier, resulting in a more densely packed dendritic structure, leading to smaller and more uniform grain sizes and increased functionality. Interestingly, this effect was only observed for loadings > 0.5 monolayers, which limits the statistical distance between particles to the size of the NPs. In contrast, $ZrB_2$ resulted in uniformly distributed grain sizes at much lower mass loadings with even more compact dendritic arms. However, no effect on functionality was observed, suggesting that the nanoparticles may be stabilizing phases that are harmful to hard magnetic functionality. It should be noted that only 100 nm $ZrB_2$ NPs were investigated in this study.

## Materials and Methods

This study used a gas-atomized Nd-Fe-B-based spherical powder manufactured by Neo Magnequench (Tuebingen, Germany). The powder is commercially known as MQP-S-11-9-20001 (hereafter referred to as MQP-S) with a declared chemical composition of Nd7.5Pr0.7Zr2.6Ti2.5Co2.5Fe75B8.8 at% [33]. The powder size distribution and morphology were characterized by scanning electron microscopy (SEM, Philips ESEM-XL30 FEG, 20kV) equipped with an energy-dispersive X-ray detector (EDX) used to evaluate the material composition and oxidation behavior. The initial powder composition was measured by X-ray fluorescence (XRF, Bruker's S8 Tiger WD-XRF) under inert gas conditions (He atmosphere). The true density of the powder was measured using a pycnometer (Borosilicate glass 3.3. DIN ISO 3507, BRAND 25 ml type Gay-Lussac).

The nano-additivation of the MQP-S powders is performed by adding laser-generated Ag NPs and $ZrB_2$ NPs, respectively, to the surface of the micrometer-sized MQP-S particles. The Ag NPs were prepared by laser ablation in liquids (LAL) [34], where the laser ablated the surface of Ag-target (20mm (width) x 80mm (length) x 2mm(thickness)) immersed in water containing 0.1 µg/L NaOH stabilizer. For the laser ablation of the Ag NPs a ps-pulsed laser (500flex, Amphos, Herzogenrath, Germany) with 150 W average output power was used. The fundamental wavelength was 1030 nm, with a laser pulse duration of 3 ps and a pulse repetition rate of 5 MHz. A galvanometer scanner (intelliSCAN-20, Scanlab AG, Purchheim, Germany) with a scanning speed of 5 m/s and an F-theta lens focusing optics f=254 mm was employed. The $ZrB_2$ NPs were prepared by laser fragmentation in liquids (LFL), using a ps-pulsed laser (TruMicro, Trumpf) with 30 W average output power on the same target material for up to 20 times. The wavelength was 515 nm, with a laser pulse duration of 10 ps and a pulse repetition rate of 100 kHz. Note, that no scanner is required for LFL, but to homogeneously distribute the NPs in the colloid, a 5-minute ultrasonic bath is required. The hydrodynamic size of the synthesized NPs was measured by analytical disc centrifugation (ADC, CPS instruments, INC) at a centrifugation speed of 24,000 rpm with a lower detection limit of 5 nm.

The MQP-S surface nano-functionalization was performed by directly mixing the powder with the colloid and post-processing to ensure the nanoparticle deposition, i.e. pH control and centrifugation. This methodology has been previously employed for the formation of

heterogeneous catalysts [35] and the preparation of nano-functionalized steel powders to manufacture ODS steels by additive manufacturing techniques [36] The pH of the MQP-S-Ag colloid mixture was modified to pH 7.0 followed by centrifugation at 4000 rpm and 10˚ C for 15 minutes. After separating the nano functionalized MQP-S powder and the supernatant, the powder is finally dried in a vacuum oven at 40 ˚C.

The prepared powder is processed by suction casting to emulate, with a lower powder amount, the high cooling rate and microstructure of PBF-LB processed samples. To prepare the powder for the suction casting system employed (Buehler MAM-1 arc melter), the Ag-MQP-S powder was pre-pressed into a copper crucible. An electric arc then melted the material, struck under a protective Ar atmosphere, and sucked into a water-cooled mold into bulk rectangular plates with a thickness of 0.5 mm. A heat treatment is applied to increase the coercivity of the manufactured parts. First, the samples are annealed at 1000 °C for 5 h with subsequent cooling in air. Then, a second annealing at 500 °C for 3 h is applied and the material is cooled down in the furnace. To determine the magnetic performance of the developed magnets, isothermal magnetization measurements were performed using a physical property measurement system (PPMS-VSM, Quantum Design PPMS-14) at room temperature under an applied magnetic field of up to 3 T.

To obtain grain orientation data, electron backscatter diffraction (EBSD) analyses were performed using a FEG-SEM (Tescan Mira3), operating at 30 kV with a step size of 0.1 µm. For each sample, three maps with an area of 60 x 140 µm² were analyzed. A neighbor pattern averaging and re-indexing (NPAR®) post-processing routine was applied to improve the indexing rate using the software OIM Analysis 8.6 (EDAX).

## Acknowledgments

This work was financially supported by the Deutsche Forschungsgemeinschaft (DFG, German Research Foundation) within the Collaborative Research Centre / Transregio (CRC/TRR) 270, Project ID No. 405553726, subprojects A08, A10, A11, Z02.

## Conflicts of interest

The authors declare no conflicts of interest.

## References


[1] Y. Kok *et al.*, "Anisotropy and heterogeneity of microstructure and mechanical properties in metal additive manufacturing: A critical review," *Mater. Des.*, vol. 139, pp. 565–586, Feb. 2018, doi: 10.1016/j.matdes.2017.11.021.

[2] T. DebRoy *et al.*, "Additive manufacturing of metallic components – Process, structure and properties," *Prog. Mater. Sci.*, vol. 92, pp. 112–224, Mar. 2018, doi: 10.1016/j.pmatsci.2017.10.001.

[3] F. H. Kim and S. P. Moylan, "Literature review of metal additive manufacturing defects," National Institute of Standards and Technology, Gaithersburg, MD, NIST AMS 100-16, May 2018. doi: 10.6028/NIST.AMS.100-16.

[4] J. M. D. Coey, "Perspective and Prospects for Rare Earth Permanent Magnets," *Engineering*, vol. 6, no. 2, pp. 119–131, Feb. 2020, doi: 10.1016/j.eng.2018.11.034.

[5] S. Pauly, P. Wang, U. Kühn, and K. Kosiba, "Experimental determination of cooling rates in selectively laser-melted eutectic Al-33Cu," *Addit. Manuf.*, vol. 22, pp. 753–757, Aug. 2018, doi: 10.1016/j.addma.2018.05.034.

[6] K. Kempen, L. Thijs, J. Van Humbeeck, and J.-P. Kruth, "Mechanical Properties of AlSi10Mg Produced by Selective Laser Melting," *Phys. Procedia*, vol. 39, pp. 439–446, 2012, doi: 10.1016/j.phpro.2012.10.059.

[7] K. Zyguła, B. Nosek, H. Pasiowiec, and N. Szysiak, "Mechanical properties and microstructure of AlSi10Mg alloy obtained by casting and SLM technique," 2018.

[8] F. Trevisan *et al.*, "On the Selective Laser Melting (SLM) of the AlSi10Mg Alloy: Process, Microstructure, and Mechanical Properties," *Materials*, vol. 10, no. 1, p. 76, Jan. 2017, doi: 10.3390/ma10010076.

[9] A. Arabi-Hashemi, X. Maeder, R. Figi, C. Schreiner, S. Griffiths, and C. Leinenbach, "3D magnetic patterning in additive manufacturing via site-specific in-situ alloy modification," *Appl. Mater. Today*, vol. 18, p. 100512, Mar. 2020, doi: 10.1016/j.apmt.2019.100512.

[10] V. Chaudhary, S. A. Mantri, R. V. Ramanujan, and R. Banerjee, "Additive manufacturing of magnetic materials," *Prog. Mater. Sci.*, vol. 114, p. 100688, Oct. 2020, doi: 10.1016/j.pmatsci.2020.100688.

[11] L. Schäfer *et al.*, "Design and Qualification of Pr–Fe–Cu–B Alloys for the Additive Manufacturing of Permanent Magnets," *Adv. Funct. Mater.*, vol. 31, no. 33, p. 2102148, Aug. 2021, doi: 10.1002/adfm.202102148.

[12] Y. M. Wang *et al.*, "Additively manufactured hierarchical stainless steels with high strength and ductility," *Nat. Mater.*, vol. 17, no. 1, pp. 63–71, Jan. 2018, doi: 10.1038/nmat5021.

[13] C. Huber *et al.*, "Coercivity enhancement of selective laser sintered NdFeB magnets by grain boundary infiltration." arXiv, Mar. 06, 2019. Accessed: May 04, 2023. [Online]. Available: http://arxiv.org/abs/1903.02233

[14] J. Fidler and T. Schrefl, "Overview of Nd–Fe–B magnets and coercivity (invited)," *J. Appl. Phys.*, vol. 79, no. 8, p. 5029, 1996, doi: 10.1063/1.361565.

[15] J. H. Martin, B. D. Yahata, J. M. Hundley, J. A. Mayer, T. A. Schaedler, and T. M. Pollock, "3D printing of high-strength aluminium alloys," *Nature*, vol. 549, no. 7672, pp. 365–369, Sep. 2017, doi: 10.1038/nature23894.

[16] I. M. Kusoglu *et al.*, "Nanoparticle Additivation Effects on Laser Powder Bed Fusion of Metals and Polymers—A Theoretical Concept for an Inter-Laboratory Study Design All Along the Process Chain, Including Research Data Management," *Materials*, vol. 14, no. 17, p. 4892, Aug. 2021, doi: 10.3390/ma14174892.

[17] T. S. Zhao, Y. B. Kim, and W. Y. Jeung, “Magnetic properties and microstructure of NdFeB sintered magnets by the addition of Ag powder,” *IEEE Trans. Magn.*, vol. 36, no. 5, pp. 3318–3320, Sep. 2000, doi: 10.1109/20.908784.
[18] H. Chen, X. Yang, L. Sun, P. Yu, X. Zhang, and L. Luo, “Effects of Ag on the magnetic and mechanical properties of sintered NdFeB permanent magnets,” *J. Magn. Magn. Mater.*, vol. 485, pp. 49–53, Sep. 2019, doi: 10.1016/j.jmmm.2019.04.071.
[19] J. Jaćimović *et al.*, “Net Shape 3D Printed NdFeB Permanent Magnet: Net Shape 3D Printed NdFeB Permanent Magnet,” *Adv. Eng. Mater.*, vol. 19, no. 8, p. 1700098, Aug. 2017, doi: 10.1002/adem.201700098.
[20] D. Goll, F. Trauter, T. Bernthaler, J. Schanz, H. Riegel, and G. Schneider, “Additive Manufacturing of Bulk Nanocrystalline FeNdB Based Permanent Magnets,” *Micromachines*, vol. 12, no. 5, p. 538, May 2021, doi: 10.3390/mi12050538.
[21] H. Rumpf, “Die Wissenschaft des Agglomerierens,” *Chem. Ing. Tech. - CIT*, vol. 46, no. 1, pp. 1–11, Jan. 1974, doi: 10.1002/cite.330460102.
[22] P. Kanninen, C. Johans, J. Merta, and K. Kontturi, “Influence of ligand structure on the stability and oxidation of copper nanoparticles,” *J. Colloid Interface Sci.*, vol. 318, no. 1, pp. 88–95, Feb. 2008, doi: 10.1016/j.jcis.2007.09.069.
[23] A. Letzel *et al.*, “Effect of various dispersing agents on the stability of silver microparticle dispersion and the formulation of uniform silver film by laser melting,” *J. Laser Appl.*, vol. 28, no. 4, p. 042004, Nov. 2016, doi: 10.2351/1.4955011.
[24] S. Rajendrachari, B. E. K. Swamy, S. Reddy, and D. Chaira, “Synthesis of Silver Nanoparticles and their Applications,” vol. 5, no. 4, 2013.
[25] R. Cao, L. Zhu, H. Liu, X. Yang, H. Nan, and W. Li, “Improvement of corrosion resistance and magnetic properties for sintered NdFeB by alumina sol-containing conversion film,” *RSC Adv.*, vol. 6, no. 95, pp. 92510–92519, 2016, doi: 10.1039/C6RA19531H.
[26] M. Gergoric, “Hydrometallurgical Treatment of Neodymium Magnet Waste”.
[27] L. Schäfer *et al.*, “A Novel Magnetic Hardening Mechanism for Nd-Fe-B Permanent Magnets Based on Solid-State Phase Transformation,” *Adv. Funct. Mater.*.
[28] A. Kirchner, W. Grünberger, O. Gutfleisch, V. Neu, K.-H. Müller, and L. Schultz, “A comparison of the magnetic properties and deformation behaviour of Nd-Fe-B magnets made from melt-spun, mechanically alloyed and HDDR powders,” *J. Phys. Appl. Phys.*, vol. 31, no. 14, pp. 1660–1666, Jul. 1998, doi: 10.1088/0022-3727/31/14/008.
[29] J. M. D. Coey, “Magnetism and Magnetic Materials”.
[30] T. N. Lamichhane, L. Sethuraman, A. Dalagan, H. Wang, J. Keller, and M. P. Paranthaman, “Additive manufacturing of soft magnets for electrical machines—a review,” *Mater. Today Phys.*, vol. 15, p. 100255, Dec. 2020, doi: 10.1016/j.mtphys.2020.100255.
[31] F. Bittner, J. Thielsch, and W.-G. Drossel, “Laser powder bed fusion of Nd–Fe–B permanent magnets,” *Prog. Addit. Manuf.*, vol. 5, no. 1, pp. 3–9, Mar. 2020, doi: 10.1007/s40964-020-00117-7.
[32] M. Skalon *et al.*, “Influence of Melt-Pool Stability in 3D Printing of NdFeB Magnets on Density and Magnetic Properties,” *Materials*, vol. 13, no. 1, p. 139, Dec. 2019, doi: 10.3390/ma13010139.
[33] Magnequench, “Datasheet MQP-S-11-9-20001.”
[34] D. Zhang, B. Gökce, and S. Barcikowski, “Laser Synthesis and Processing of Colloids: Fundamentals and Applications,” *Chem. Rev.*, vol. 117, no. 5, pp. 3990–4103, Mar. 2017, doi: 10.1021/acs.chemrev.6b00468.

[35] G. Marzun, J. Nakamura, X. Zhang, S. Barcikowski, and P. Wagener, “Size control and supporting of palladium nanoparticles made by laser ablation in saline solution as a facile route to heterogeneous catalysts,” *Appl. Surf. Sci.*, vol. 348, pp. 75–84, Sep. 2015, doi: 10.1016/j.apsusc.2015.01.108.

[36] C. Doñate-Buendia *et al.*, “Microstructure formation and mechanical properties of ODS steels built by laser additive manufacturing of nanoparticle coated iron-chromium powders,” *Acta Mater.*, vol. 206, p. 116566, Mar. 2021, doi: 10.1016/j.actamat.2020.116566.

[37] S.-X. Liang, L.-C. Zhang, S. Reichenberger, and S. Barcikowski, “Design and perspective of amorphous metal nanoparticles from laser synthesis and processing,” *Phys. Chem. Chem. Phys.*, vol. 23, no. 19, pp. 11121–11154, 2021, doi: 10.1039/D1CP00701G.

[38] R. Streubel, S. Barcikowski, and B. Gökce, “Continuous multigram nanoparticle synthesis by high-power, high-repetition-rate ultrafast laser ablation in liquids,” *Opt. Lett.*, vol. 41, no. 7, p. 1486, Apr. 2016, doi: 10.1364/OL.41.001486.

[39] E. Fazio *et al.*, “Nanoparticles Engineering by Pulsed Laser Ablation in Liquids: Concepts and Applications,” *Nanomaterials*, vol. 10, no. 11, p. 2317, Nov. 2020, doi: 10.3390/nano10112317.

# Supporting information

**<u>Section I:</u> Laser ablation in liquids process:** The technique of laser ablation in liquid (LAL) was first described by A. Fojtík and A. Henglein for simple and surfactant-free nanoparticle synthesis [37]. In contrast to wet chemical methods, laser synthesis does not demand the employment of chemical precursors and organic surfactants. LAL requires the delivery of a high energy density to the target material in order to overcome the ablation threshold and promote material removal from the target surface. The removed material is collected in the surrounding liquid forming a colloidal dispersion of nanoparticles. In order to overcome the ablation threshold while reducing the laser's interaction with the surrounding liquid, short and ultrashort laser pulses in the range of fs up to ns are employed instead of continuous wave lasers that suffer from strong heating of the liquid [38]. The LAL process outcome is determined by various parameters, including material and laser features [39]. Another advantage of LAL is the reduction of byproducts in the colloids, allowing the direct employment of the generated nanoparticles without further purification steps. This is particularly appropriate for the Ag nanoparticles generated in the current work that is added to MQP-S powder by pH-controlled dielectrophoretic deposition. The process is proven to reduce nanoparticle agglomeration during nanoparticle support.

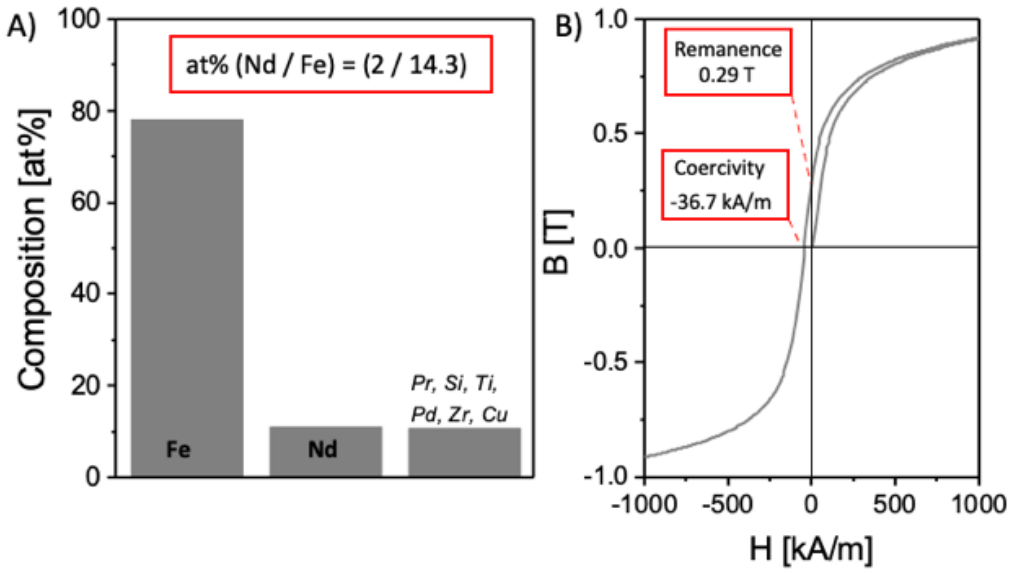


*Figure S 1 Properties of non-additive MQP-S powder: A) chemical composition; B) half hysteresis loop with the initial magnetization curve.*

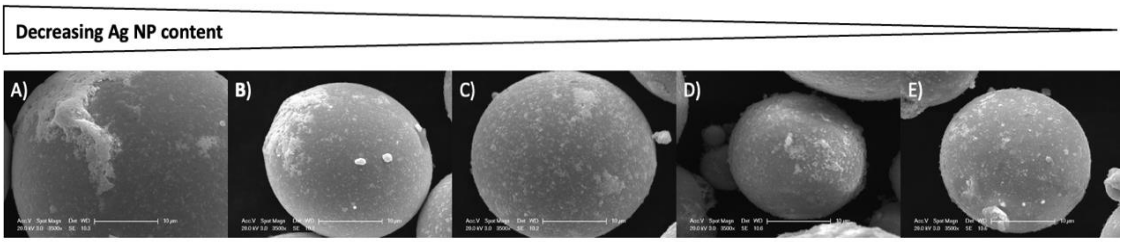


*Figure S 2 BSE images of Ag NPs modified powder with different mass load.*

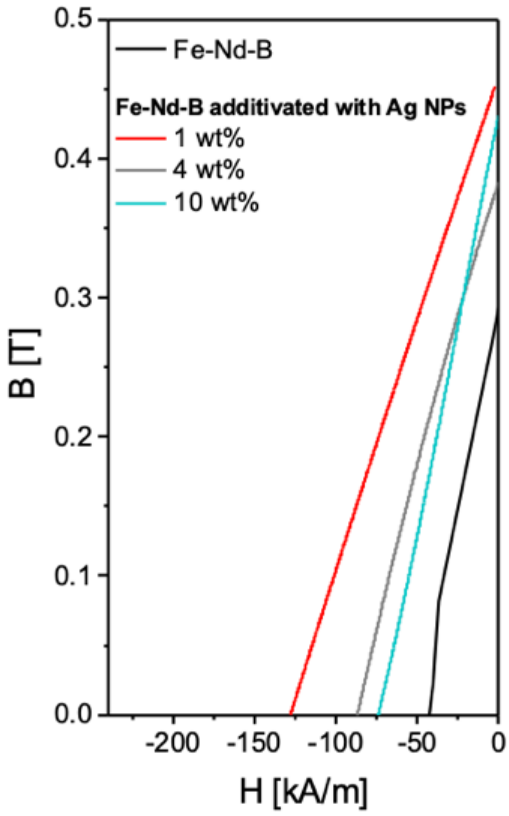


*Figure S 3 Demagnetization curve of annealed suction casting flakes from: non-modified powder and Ag NPs modified powder with different mass load.*